Nonlinear optical studies of single gold nanoparticles

Dijk, M.A. van

4

Acoustic vibrations of single gold nanoparticles

4.1 Introduction

The confinement of electrons and phonons causes the physical properties of nanometer-sized objects to depart from those of bulk solids [28]. One of the ambitions of nanoscience is to exploit these deviations to tailor the properties of nanoparticles through their sizes and shapes. The plasmon resonance of noble-metal (silver and gold) particles is a collective oscillation of the conduction electrons, which governs their strong interaction with light. The shift and broadening of the plasmon resonance with changes in size and shape remains an active research area [16, 17, 75]. A further strong motivation for optical studies of metal nanoparticles is their recently proposed use as labels for molecular biology [13, 54, 59, 85].

Working with ensembles of nanoparticles entails a fundamental difficulty. The current preparation methods generate a distribution of particles with a significant dispersion of sizes and shapes, and with many possible configurations of defects. This problem can be solved by the isolation of *single* nanoparticles. A number of methods have recently been put forward to study them with near-field [100] and far-field optical microscopy [87]. Each single nanoparticle can be studied in detail, and extended statistics can then be accumulated over many individuals. Following one and the same particle gives access to environmental influences and unravels space and time heterogene-

ity. In this chapter, we show different electronic and elastic components in the time-resolved response of single gold nanoparticles. Combining short laser pulses with the microscopy of single nano-objects (molecules [101], semiconductor [102], or metal particles) offers new insight into their optical and mechanical properties on their characteristic times, picoseconds and shorter.

When an ultrashort pump pulse excites a metal particle, the absorbed energy is first conveyed to the conduction electrons, which collide within some tens of femtoseconds through electron-electron interactions [16, 17, 75]. On a 1-ps timescale, the hot electrons thermalize with the lattice, and, still later (typically 10 ps for a 10-nm particle), the whole particle cools down to ambient temperature via heat diffusion. The sudden heating of the electron gas has mechanical effects. Just as sharp rap causes a bell to ring, an optical excitation launches elastic oscillations, via two mechanisms: First, a short-lived transient arises from the initial surge in electronic temperature and Fermi pressure. This pressure burst is short but strong because of the low heat capacity of the electron gas [44]. Second, as the electronic energy is shared with lattice modes on a picosecond timescale, anharmonicity leads to thermal expansion. For large enough particles, both times are short compared to the period of elastic vibrations (3.3 ps for the breathing of a 10-nm diameter particle).

The optical properties of the hot particle are also modified. The initial excitation spreads the electronic population around the Fermi level, thereby opening new relaxation channels and broadening the surface plasmon resonance [52]. The subsequent thermal expansion of the lattice reduces the electron density, bringing about a red shift of the plasmon resonance. Size variations can thus be optically detected via shifts of the plasmon resonance. In particular, the elastic oscillations that are launched in a particle by a short pulse, are optically detectable through a periodic red shift of the plasmon resonance.

Laser-induced acoustic vibrations of nanoparticles have been previously studied on ensembles [16, 17]. Such bulk observations are only possible as long as the oscillations are synchronized. Small differences in particle size within the ensemble lead to slight differences in oscillation periods. This inhomogeneous broadening, which often dominates the observed decay of the ensemble oscillation, is completely eliminated in our present study of single gold nanoparticles by interferometric pump-probe spectroscopy.

4.2 Experimental method

As a single nanoparticle is much smaller than the diffraction-limited laser spot, and as time-dependent changes in optical properties are small, the signals are weak. Measuring minute absorption changes requires many photons and the reduction of all noise sources, down to photon-noise. An interferometer set close to its dark fringe suppresses intensity fluctuations on all timescales. We designed a common-path interferometer, in which two interfering pulses follow the same optical path at different times and with orthogonal polarizations (Fig. 3.1 on page 48). Defects of the optical components (particularly of the objectives), being nearly identical for both polarizations, cancel to a large extent. The setup is described in detail in chapter 3. A short description follows.

The measuring light pulse is linearly polarized at 45 degrees from vertical and split into probe and reference pulses by a first birefringent crystal (calcite). The reference pulse is polarized along the crystal's horizontal fast axis, and the probe along the vertical slow axis. The pump pulse, being polarized along one of the crystal axes, is not split, and travels at a variable delay from the reference-probe pulse pair. After passage through the microscope, reference and probe pulses are recombined in a second, identical calcite crystal, with its fast axis vertical. Crystals as splitting elements have the advantage that alignment is easy, but the time delay (10 ps) is fixed by their thickness.

A pump-induced change in the real or imaginary part of the particle's dielectric permittivity causes a small variation $\Delta\zeta$ in the probe field's complex amplitude, from E to $(1 + \Delta\zeta)E$. This change is detected by the interferometer, either as an amplitude or as a phase variation. The working point of the interferometer is adjusted by independently rotating a quarter-wave plate and a polarizer. The amplitude-sensitive working point is obtained for slightly different amplitudes but equal phases of the interfering waves, and gives the variations of the real part $\mathrm{Re}(\Delta\zeta)$ of the probe field. At the phase-sensitive working point, the amplitudes are equal and the phases are slightly different, giving $\mathrm{Im}(\Delta\zeta)$. In the following, unless mentioned, we use the amplitude-sensitive working point.

The Fourier-limited 1-ps probe pulses are generated at a 76 MHz rate by an intra-cavity frequency-doubled optical parametric oscillator (OPO), tunable between 520 and 650 nm. The OPO itself is pumped at 800 nm by the 1-ps pulses of a Ti:sapphire laser. A small fraction of the latter beam, used as pump, is modulated at 400 kHz by an acousto-optical modulator (AOM). The probe (and reference) power varied between 12 and 330 μW, the pump power between 0.5 and 5 mW. The home-built microscope includes an oil-

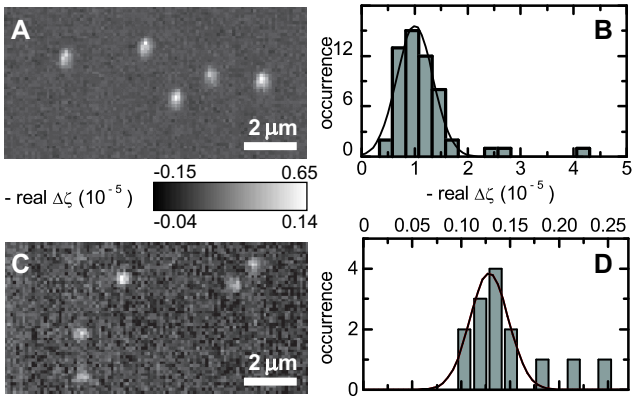

Figure 4.1: Raster-scanned images of single gold nanoparticles and corresponding histograms of field changes $\mathrm{Re}(\Delta\zeta)$ for 20 nm (A,B) and 10 nm diameter (C,D). The integration times were 100 and 200 ms/pixel, respectively. A minimum signal level was required to start the fit to a Gaussian spot, indicated by a dashed line in the histograms. The relative width of the distributions, as deduced from rough Gaussian fits, is 34 % (20 nm) and 11 % (10 nm). The noise level in panel (C) is $7.1 \cdot 10^{-5}$, less than three times the shot-noise limit.

immersion objective (numerical aperture NA=1.4), and an air-spaced objective (NA=0.95). The measurement spot has a 300 nm diameter. The sample cover slide, mounted on a piezo stage, can be scanned with 25 nm precision. The interferometer output is fed to an analog avalanche photodiode and demodulated in a lock-in amplifier.

The samples are roughly spherical gold particles with diameters ranging between 10 nm and 80 nm (British Biocell International and Sigma-Aldrich), spin-coated with a poly(vinyl alcohol) solution (10 g/l) on a clean glass cover slide (see section 3.2 for a description of the glass-cleaning procedure) . The polymer film was about 20 nm thick.

Please note that on the axes of the figures in this and the next chapter we have plotted - Re($\Delta\zeta$), contrary to our publications. This is caused by a late discovery of a mistake of 180° in the phase setting of our lock-in amplifier. This mistake had been made consistently in all plots. We have decided to make a correction to the axes and not to the traces. The convention of plotting - Re($\Delta\zeta$) has been kept for the unpublished data as well.

4.3 Imaging single gold nanoparticles

Figure 4.1 shows images of single gold nanoparticles with 10 and 20 nm diameter. The sample preparation procedure was that of chapter 2, where third-harmonic signals proved that the particles were isolated. Figure 4.1 is recorded for zero delay, i.e., when the pump and probe pulses impinge simultaneously on the sample, providing maximum contrast. We extracted histograms from a set of images, as done in Chapter 2. The discrimination threshold between noise and particles was $\mathrm{Re}(\Delta\zeta) = -2.7 \cdot 10^{-4}$ (B) and $-1.3 \cdot 10^{-4}$ (D). The resulting distributions, shown in Fig. 4.1B and D, being mono-modal and well separated from the background, confirm that each spot corresponds to a single particle. The relative width of the 20-nm distribution, 34%, is considerably larger than expected from the volume spread given by the manufacturer (19%). Additional fluctuations in shape, orientation and surroundings of the particles can contribute to this large dispersion via shifts and intensity changes of the plasmon resonance, as recently observed by Berciaud et al. [60]. In order to minimize the spread in signal, we recorded the data of Fig. 4.1 with an off-resonant probe (635 nm). Pump and probe power were limited by the maximum permissible absorption in the particle, which results in a detection limit of 10-nm diameter for gold nanoparticles, for reasonable sampling times shorter than one second per pixel.

4.4 Time-resolved experiments

We measure the time-dependent response of the nanoparticle to excitation with the pump pulse by varying the delay between the pump pulse and the probe-reference pair of pulses. Fig. 4.2 shows an example of the response of a single 60-nm gold nanoparticle in the laser focus, detected with a bandwidth of 7.8 Hz. The first part of the trace, which is enlarged in the inset, shows two sharp peaks, that occur when the pump is overlapped with the probe and with the reference respectively. These peaks stem from the change in optical response due to the hot electron gas. From the rise and decay times of the peaks, the electron-electron scattering and electron-phonon coupling times can be obtained [17, 103]. Since these processes take place on timescales faster than a picosecond, the width of the peaks is dominated by the pulse length if the measurement is carried out with picosecond pulses, and information on the electronic decay times of the particle is lost. However, by using shorter pulses, it is possible to resolve these processes. This is demonstrated in the

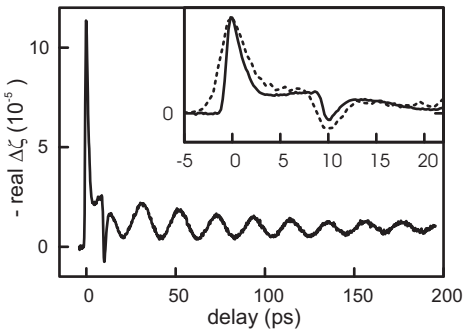

Figure 4.2: Example of a delay scan of a single 60-nm gold nanoparticle showing a short spike due to the hot electron gas and periodic oscillations of the particle size. The inset compares the 'femtosecond' (solid) and the 'picosecond' (dashed) configuration of the laser system in their resolving power of the fast electronic process. The traces in the inset are normalized to the first peak. The detection bandwidth was 7.8 Hz.

inset of Fig. 4.2, where the fast electronic response is measured with femtosecond and picosecond pulses on two different single particles. In the femtosecond experiment, the peaks are narrow enough to resolve the electronic processes in the particle. On a longer timescale, the signal shows a damped harmonic oscillation. This is a direct observation of the acoustic vibrations of the particle, from which we can derive information on the elastic properties of the particle itself and its mechanical coupling to the surroundings.

As mentioned in section 4.1, the optical detection of acoustic vibrations is assumed to be caused by a periodic red shift of the plasmon resonance, caused by a periodic change of the electron density. Figure 4.3 shows two delay scans, one with the probe tuned to the red wing (595 nm) and one to the blue wing (520 nm) of the particle's resonance. The oscillations are out of phase, which gives clear evidence for this periodic red shift, as has also been seen earlier in bulk experiments on silver nanoparticles [104].

In Fig. 4.4, we combine the amplitude and phase separation with time-resolved experiments, in order to measure the complete complex temporal response of the particle. As mentioned in section 3.3, for delay times larger than 10 ps, it is important to choose a working point close to the dark fringe, to ensure the full separation of amplitude and phase. The interferometer was tuned to a 2% fringe, to comply with the approximation of Eq. (3.2). In Fig. 4.4A, the real and imaginary temporal responses of a single particle are shown together. Here, the different spectral origin (resonance broadening

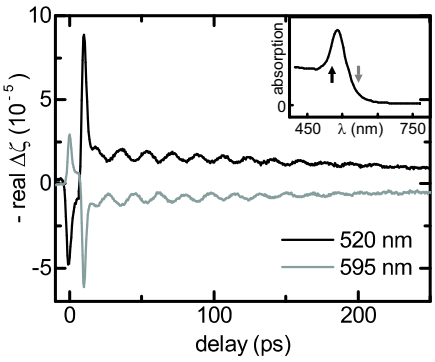

Figure 4.3: Two delay scans of one single gold particle, with the probe on the red side (black trace) and on the blue side (grey trace) of the surface plasmon resonance (see inset). The period of the oscillations is 17.6 ps for both traces, corresponding to a particle size of 53 nm [17].

versus red shift) of the peaks and of the oscillations becomes apparent, since the two peaks have the same sign in both the amplitude and the phase configuration, while the vibrations are exactly out of phase. Figure 4.4B shows the real and imaginary temporal response of another particle in the same sample. While the amplitude response of this particle is nearly the same as that of the particle in Fig 4.4A, the phase response is rather different. The electronic contribution gives a mainly dispersive response, while the acoustic vibrations are completely absorptive. The differences between the two particles can be visualized in a different manner in Fig. 4.4C, where the dispersive response is plotted against the absorptive response for both particles. The trace of the particle from Fig. 4.4A (gray) shows a weaker electronic response, while the overall trace is tilted towards the real axis. These kind of differences between particles can arise from differences in their spectral responses, themselves due to differences in their size, shape or local environment. Further study is needed to precisely correlate the optical and structural properties of the particles, but there is little doubt that single-particle studies of gold nanoparticles will lead to a better understanding of their properties, and to such applications as elasticity and damping sensors at nanometer scales.

Because of their size and shape distribution, individual particles present slightly different oscillation periods, and they run out-of-phase on longer timescales. This inhomogeneous broadening of the breathing mode totally masks any intrinsic damping of the ensemble oscillation. Selecting a single particle provides direct access to the intrinsic (or homogeneous) damping, by

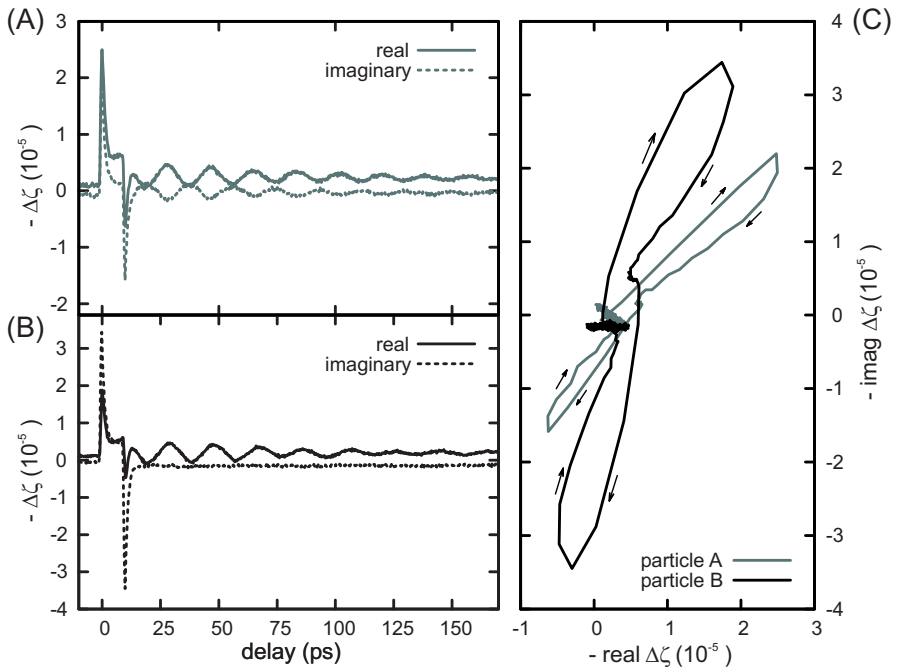

Figure 4.4: (A,B) Delay scans of two gold nanoparticles with a nominal diameter of 60 nm, measured at the amplitude (solid) and phase (dotted) sensitive working point. For particle (A), the peaks have the same sign, but the sign of the vibrations is opposite demonstrating the different spectral origin. For the particle in panel (B), the dispersive contribution to the peaks is much stronger, while the vibrations completely vanish in this phase-sensitive configuration. (C) Plotting $\mathrm{Im}(\Delta\zeta)$ against $\mathrm{Re}(\Delta\zeta)$ reveals the full response of both particles in the complex plane. The arrows indicate the time evolution. In all plots, the detected intensity was 2% of the bright-fringe intensity. The traces show the average of five measurements, each with a detection bandwidth of 7.8 Hz.

removing ensemble averaging. The damping rate is found to vary from particle to particle, probably through fluctuations of the environment and of the coupling to acoustic phonons in the substrate. The resonance quality factors $Q = \nu/\Delta\nu$ ($\Delta\nu$ being the mode's FWHM in the power spectrum), are about 4-5 for an ensemble, but reach considerably larger values, distributed between 15 and 30 (corresponding to amplitude $1/e$ relaxation times of 75-150 ps), for individual particles in the thin polymer film.

A striking illustration of the strength of single-particle observations is displayed in Fig. 4.5. The left panel shows delay scans and the right panel shows

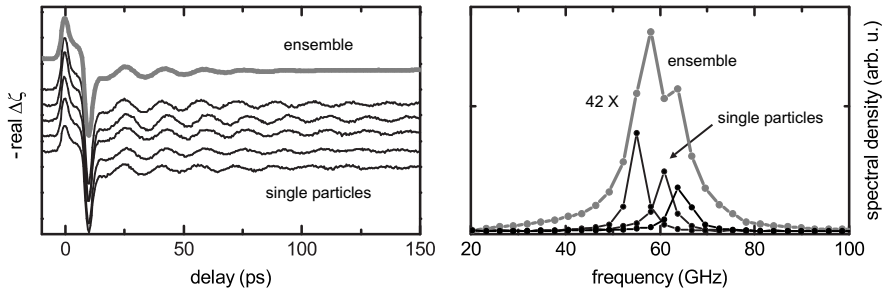

Figure 4.5: Comparison of delay scans (left panel) and power spectra of the oscillatory part (right panel) of a set of 29 single gold nanoparticles (examples shown as thin black lines) to a reconstructed ensemble measurement (thick grey line; for this experiment, the sample was covered by index-matching fluid, which increased the damping of the oscillations). The particles have a nominal size of 50 nm with a spread of 6 %. The sample was prepared as described in this chapter and additionally coated with an index-matching fluid. The average spectrum in part (B) is scaled by 42 for clarity. The quality factor $Q = \nu/\Delta\nu$ is 4 for the ensemble and about 13 for the individual traces. The index-matching fluid reduces the quality factor of the individual traces compared to particles embedded in a thin polymer film only (see main text).

power spectra of the oscillatory behavior of nanoparticles. We measured 29 single particles under the same experimental conditions and then calculated an average trace to yield an "ensemble" signal (thick grey line). Examples of the single particle data are shown as thin black lines. Comparing the "ensemble" signal to the single particle signal, we clearly see that the ensemble oscillation damps much faster than those of individual nanoparticles, and as a result, the peak in the ensemble power spectrum is much broader, as can be seen in the right panel of Fig. 4.5. Because of the size distribution, the nanoparticles present slightly different oscillation periods, and they run out-of-phase on longer timescales. This inhomogeneous broadening easily masks the intrinsic decay of the vibrations of individual particles.

4.5 Vibrational modes

The elastic vibration modes of a solid sphere are labelled in Lamb's theory [46] by two integers, n, the harmonic order, i.e., the number of radial nodes, and l, the angular momentum number, which represents the angular dependence of the mode. We calculated the mode frequencies using bulk gold transversal and longitudinal sound velocities [50] following the equations

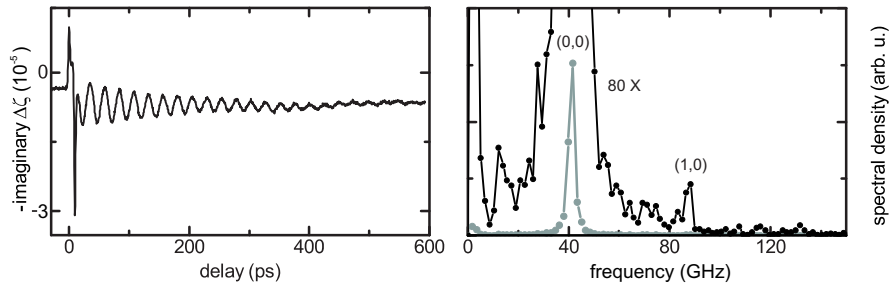

Figure 4.6: Delay scan of a single 80-nm particle, which shows the second harmonic $(n,l) = (1,0)$ of the fundamental breathing mode at $\Omega_{1,0} \approx 2.17 \cdot \Omega_{0,0}$, close to the expected value of Lamb's theory at $2.103 \cdot \Omega_{0,0}$. The delay trace (left panel) has no signs of higher harmonics, but the power spectrum (right panel) shows a clear peak at $\Omega_{1,0}$.

given in Ref. [46] for free boundary conditions. Most of the particles only show the radial breathing mode $(n,l) = (0,0)$ at a frequency $\Omega_{0,0}$, sometimes with a weak trace of the higher harmonic $(n,l) = (1,0)$ at about $2.1 \cdot \Omega_{0,0}$, as seen in ensemble measurements for silver nanoparticles [105]. An example of a detected second harmonic is shown in Fig. 4.6. Other particles show an additional mode at a lower frequency. Fig. 4.7A shows an example, where the time-response clearly deviates from a sine-curve. The power spectrum obtained by Fourier transformation of the oscillation (Fig. 4.7B, top trace) shows two distinct peaks. The high-frequency peak (at 67 GHz for the upper spectrum) corresponds to the spherical breathing mode $(n,l) = (0,0)$ of a 45 nm diameter gold sphere [17]. Another peak appears at lower frequency (28 GHz for the upper spectrum). This new peak cannot arise from the breathing mode of a second, larger particle at the same spot, for the optical signal (which scales as the third power of particle diameter) would then be too weak . We assign the peak at 28 GHz to the non-spherically symmetric $(n,l) = (0,2)$ mode, involving shear strain (uniaxial cigar-to-pancake deformations of the sphere, or ellipsoidal deformation), which was seen already in Raman spectra of semiconductor nanoparticles [46]. We rule out the lower-order $(n,l) = (0,1)$ mode, corresponding to a pear-shaped deformation, because it does not couple to the optical response, at least at the lowest order and in a spherically symmetric environment. Both modes can only be excited by the isotropic heat pulse if the spherical symmetry of the particle's expansion is broken either by the substrate, or by the particle's shape. Indeed, the $(n,l) = (0,2)$ mode does not appear in ensemble pump-probe experiments, where the particles' environment is isotropic. The measured frequency of

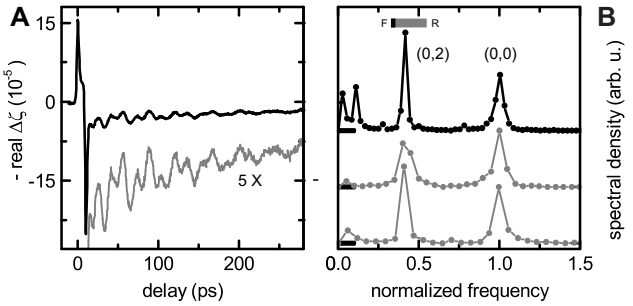

Figure 4.7: (A) Delay scan of a single gold nanoparticle. The oscillation pattern shows a complex modulation. The tail of the trace is also shown $5\times$ enlarged. (B) Power spectra of this particle's oscillation (top spectrum) and of two other particles. Frequencies and amplitudes are normalized to those of the $(0,0)$ mode (The absolute frequencies were 67 GHz, 59 GHz, 63 GHz, from top to bottom). The low frequency peak (top spectrum: 28 GHz) lies between calculated frequencies of the $(0,2)$ mode for free boundary (F, thick line on bar) and for rigid boundary (R, end of bar). The ratio of its frequency to that of the breathing mode is constant.

the $(n,l) = (0,2)$ mode lies between the frequencies expected for a sphere with free and rigid boundaries (see bar in Fig. 4.7B). The shift from the free sphere's vibration could possibly arise from elastic perturbation by the glass half-space. We note, moreover, that the ratio of $(0,2)$ to $(0,0)$ frequencies was the same for all measured particles, which rules out deviations from the spherical shape as origin of the low-frequency mode, as these would vary from particle to particle.

4.6 Conclusion

Interferometric pump-probe measurements of single metal particles have the double advantage of high sensitivity and of providing the full optical response, including phase and amplitude. We have imaged gold particles as small as 10-nm diameter, these being the detection limit of our setup, due to saturation of the absorption. The use of 100-fs pulses allows us to study electronic properties on a single-particle basis. On a longer timescale, we recorded time-traces of acoustical breathing modes, displaying particle-to-particle fluctuations in frequency and decay rate, and revealing the intrinsic damping of mechanical vibrations. We found a new mode at lower frequency, so far unobserved in pump-probe experiments, and presumably coupled by a substrate-induced breaking of the spherical symmetry. Mechanical vibra-

tion modes are fascinating doorways to the elastic properties of metal particles and of their environment. More generally, probing single nano-objects and nano-structures with short laser pulses opens a wealth of real-time studies of nano-mechanics on picoseconds, the characteristic vibration times at nanometer length scales.